Journal of Materials Chemistry A

Accepted Manuscript

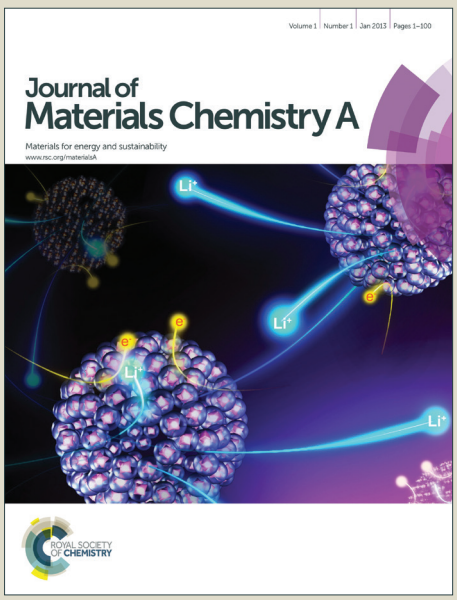

ROYAL SOCIETY OF CHEMISTRY

www.rsc.org/materialsA

Journal Name

ARTICLE

Fabrication of hierarchical porous $MnCo_2O_4$ and $CoMn_2O_4$ microspheres that are composed of polyhedral nanoparticles as promising anodes for long-life LIBs

Received 00th January 20xx,
Accepted 00th January 20xx

DOI: 10.1039/x0xx00000x

www.rsc.org/

Guangda Li,[a] Liqiang Xu,*[, b] Yanjun Zhai[b] and Yaping Hou[b]

Uniform hierarchical porous $MnCo_2O_4$ and $CoMn_2O_4$ microspheres (3-6 μm) were fabricated through solvothermal process followed by a post annealing treatment. Fascinatingly, these porous $MnCo_2O_4$ and $CoMn_2O_4$ microspheres are composed of numerous polyhedral nanoparticles with diameters in the range of 200-500 nm. The porous structure is believed beneficial for improving the lithium-storage performance of the products, which can effectively buffer the volume expansion during Li^+ insertion/extraction process and shorten the Li^+ diffusion lengths. Polyhedral structure can enhance the electrolyte/electrode contact area and increase the Li^+ insertion/extraction sites. When used as anode materials for lithium-ion batteries, the porous $MnCo_2O_4$ and $CoMn_2O_4$ microspheres exhibited excellent long-life cycling performance at high rate density. At current density of 1000 mA g^{-1}, the $MnCo_2O_4$ and $CoMn_2O_4$ exhibite initial capacity of 1034 and 1107 mAh g^{-1} and the capacity maintain at 740 and 420 mAh g^{-1} after 1000 cycles. Furthermore, the growth mechanism of porous microspheres is proposed based on many contrast experiments. The relationship between morphology evolution and annealing time is particular investigated in detail. It is find that the annealing time plays an important role to get products with different morphologies. Through controlled annealing time, porous microspheres, yolk-shell microspheres and solid microspheres could be selectively obtained.

1. Introduction

Micro-/nanostructured binary metal oxides with spinel structure (such as AB_2O_4 type) have attracted increasing attention as high capacity anode materials for next-generation lithium-ion batteries (LIBs) because of their much higher capacities than that of graphite, as well as their environmental friendly and low cost.[1-7] They usually exhibit enhanced capacities and good cycling performances owing to their complementarity and synergy effect in the insertion/extraction process as anodes for LIBs. For instance, $NiCo_2O_4$ exhibited relative better electrical conductivity and higher electrical activity compared with individual NiO and Co_3O_4. As in Mn-based or Co-based metal oxides, Co showed a higher oxidation potential than Mn, while Mn can transport more electrons and bring in higher capacity than Co.[4] Therefore, $MnCo_2O_4$ and $CoMn_2O_4$ might have prospective applications in the field of LIBs.[8,9] However, spinel structured $MnCo_2O_4$ and $CoMn_2O_4$ have received little attention as anode materials for LIBs although they have been extensively studied as magnetic,[10] catalytic,[11] supercapacitor electrode materials.[12,13] For example, multiporous $MnCo_2O_4$ and $CoMn_2O_4$ qusi-hollow spheres that are composed of irregular particles exhibited reversible capacities of 755 and 706 mAh g^{-1} at 200 mA g^{-1} after 25 cycles. Microspheres $MnCo_2O_4$ that are composed of irregular particles fabricated by a one-step solvothermal method as anode materials delivered a reversible capacity of up to 722 mAh g^{-1} after 25 cycles at 200 mA g^{-1}.[14] Although their capacities have been largely improved within 25 cycles at small current densities (200 mA g^{-1}), however, owing to the volume change and polarization effection especially at high rate density, the long cycle and high performances of $MnCo_2O_4$ and $CoMn_2O_4$ still remains a great challenge up to date.

LIBs have become one of the most important power sources for portable devices nowadays, and the development of advanced electrode materials for high-performance LIBs has been paid increasing attention along with the fast increasing energy demand in portable electronic devices and electric vehicles.[15-18] To meet the requirements of high energy density and power density and long cycling stability, extensive efforts have been focused on the fabrication of excellent anode materials with well-defined morphology and unique structures for next-generation LIBs.[19-22] Hierarchical spheres with porous or hollow structures could facilitate the entering of electrolyte and lithium ions, and could provide much more active sites compared with those of solid ones for lithium ion storage, which therefore can provide fast transport channels and reduce

[a] Key Laboratory of Processing and Testing Technology of Glass & Functional Ceramics of Shandong Province, School of Material Science and Engineering, Qilu University of Technology, Jinan 250353, China.
[b] Key Laboratory of Colloid and Interface Chemistry, Ministry of Education, School of Chemistry and Chemical Engineering, Shandong University, Jinan 250100, China. E-mail: Xulq@sdu.edu.cn; Fax: +86 531 88366280; Tel: +86 531 88364543

† Electronic Supplementary Information (ESI) available. See DOI: 10.1039/x0xx00000x

diffusion paths of Li^+ ions. The large surface area of the porous structure could promote the contact between electrode and electrolyte, and buffer the volume change during the discharge/charge cycles, thus leading to enhanced capacity and cycling performance.[23] To the best of knowledge, hierarchical porous $MnCo_2O_4$ and $CoMn_2O_4$ microspheres that are composed of polyhedral nanoparticles as promising anodes for long-life LIBs at high current density have not been reported up to date.

Herein, a facile approach for the synthesis of carbonate precursor ($Mn_{0.33}Co_{0.67}CO_3$ and $Co_{0.33}Mn_{0.67}CO_3$) yolk-shell microspheres was designed using solvothermal route by tuning the molar ratio of Mn and Co. After the carbonate precursors were calcined in air at 600 ℃ for 2 h, porous $MnCo_2O_4$ and $CoMn_2O_4$ uniform microspheres with high yields were obtained. Surprisingly, porous $MnCo_2O_4$ and $CoMn_2O_4$ microspheres are consisted of numerous polyhedral nanoparticles with diameters of 200-500 nm. The as-obtained porous $MnCo_2O_4$ and $CoMn_2O_4$ microspheres display high capacity and good cycling performance when utilized as anode materials. The first discharge capacities are 1034 and 1107 mAh g^{-1}, showing initial efficiencies of 73% and 68%, respectively. The capacities is still retained at 740 mA g^{-1} and 420 mA g^{-1} after 1000 cycles at current density of 1000 mA g^{-1}. The long cycle life at high rate capability enables the possible applications of these anode materials.

2. Experimental

2.1 Sample preparation

In a typical procedure, 2 mmol $Mn(CH_3COO)_2{\cdot}4H_2O$ and 4 mmol $Co(CH_3COO)_2{\cdot}4H_2O$ were dissolved in 45 ml ethylene glycol under vigorous stirring. Then, 1.5 g hexamethylenetetramine (HMT) was added into the above solution. The mixture system was continually stirred for 30 min to obtain a homogeneous solution and then transferred into a 60 ml Teflon-lined stainless-steel autoclave. The autoclave was sealed and heated at 180 °C for 12 h in oven. After cooling naturally, the precipitates (precursors) were collected and washed with absolute ethanol and deionized water several times, and then dried at 60 °C for 5 h in a vacuum oven. The as-obtained precursors heated in a furnace at 600 °C for 2 h in atmosphere. Finally, the porous $MnCo_2O_4$ microspheres could be obtained. For the synthesis of porous $CoMn_2O_4$ microspheres, the processes were carried out in the similar way with the prepared $MnCo_2O_4$ except that the molar ratio of $Mn(CH_3COO)_2{\cdot}4H_2O$ and $Co(CH_3COO)_2{\cdot}4H_2O$ was 1:2.

2.2 Characterization

The X-ray powder diffraction (XRD) patterns were carried out on a Bruker D8 advanced X-ray diffractometer equipped with graphite monochromatized Cu Kα radiation (λ=1.5418 Å). Fourier transform infrared (FTIR) spectra are recorded on a VERTEX-70 Fourier transmission infrared spectrometer. The morphologies of the samples were observed through field emission scanning electron microscopy (SEM) and transmission electron microscope (TEM) measurements, which were carried out on a JSM-7600F and a Hitachi H-7000 TEM instrument, respectively. High-resolution transmission electron microscope (HRTEM) images were carried out on a JEOL 2010 Transmission electron microscope with an accelerating voltage of 200 KV. The composition of the samples was analyzed by energy dispersive X-ray spectroscopy (EDX) attached to SEM and X-ray photoelectron spectra (XPS, VGESCALABMK X-ray spectrometer). N_2 adsorption/desorption isotherms were measured at 77 K on a Micromeritics ASAP 2020 volumetric adsorption system. Thermal gravimetric analysis was carried out on a Mettler Toledo TGA/SDTA851 thermal analyzer apparatus under air atmosphere.

2.3 Electrochemical measurements

The electrochemical tests were performed under ambient temperature using two-electrode coin cell (size: 2032) with lithium serving as both the counter electrode and the reference electrode. The working electrodes was prepared by mixing 70 wt% active materials ($MnCo_2O_4$ and $CoMn_2O_4$), 10 wt% Sodium Carboxy Methyl Cellulose (CMC), and 20 wt% acetylene black onto a copper foil substrate. The electrodes were dried at 100 □ in a vacuum oven for 24 h. Celgard 2400 porous polypropylene membrane was used as separator. The electrolyte consisted of a solution of 1 M $LiPF_6$ in an ethylene carbonate/dimethyl carbonate/diethyl carbonate (EC/DMC/DEC, 1:1:1, volume ratio). The cell assembly was carried out in an argon-filled glovebox with both the moisture and the oxygen content below 1 ppm. The discharge/charge tests of the samples were performed on a Land battery test system (CT2001A). The cyclic voltammetry (CV) test was carried out in the potential window of 0.01 V to 3.0 V by an electrochemical workstation (CHI 760e). The electrochemical impedance spectroscopy (EIS) was measured on an FRA-520 (MaterialsMates, Italia) connected to a Potentiostat-510 (MaterialsMates) in the frequency range from 100 KHz to 0.01 Hz.

3. Results and discussion

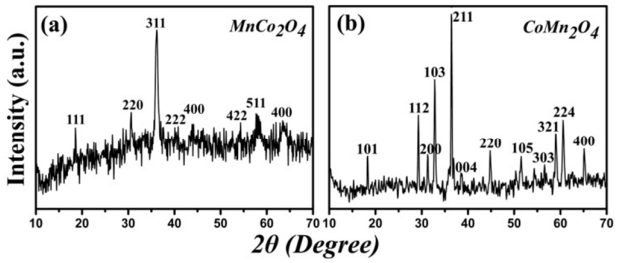

Fig. 1 XRD pattern of the porous (a) $MnCo_2O_4$ and (b) $CoMn_2O_4$ microspheres.

In this study, uniform carbonate precursors were firstly fabricated by a solvothermal method. After they were annealed at 600 ℃ for 2 h in air, porous $MnCo_2O_4$ and $CoMn_2O_4$ microspheres were obtained. The composition and phase purity of the $MnCo_2O_4$ and $CoMn_2O_4$ microspheres are examined by XRD patterns. As shown in Fig. 1, all of the diffraction peaks in this pattern can be indexed to be face-centered cubic $MnCo_2O_4$ (*a*=8.269 Å, space group *Fd3m* (227), JCPDS no. 23-

1237) and $CoMn_2O_4$ (a=5.784 Å, space group $I4_1/amd$, JCPDS no. 77-0471) with a spinel structure. No other diffraction peaks are observed, implying the high purity of the products.

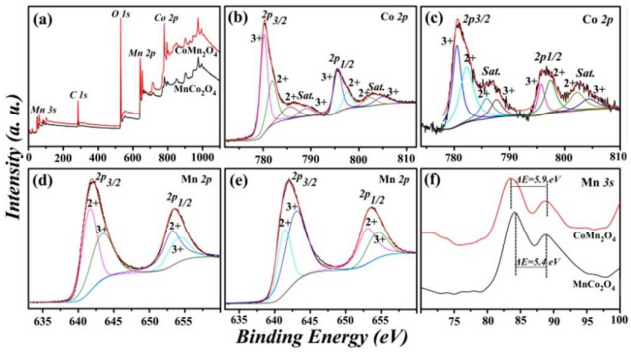

Fig. 2 XPS spectra of the porous $MnCo_2O_4$ and $CoMn_2O_4$ microspheres. (a) Survey spectrum, (b) Co 2p of the $MnCo_2O_4$, (c) Co 2p of the $CoMn_2O_4$, (d) Mn 2p of the $MnCo_2O_4$, (e) Mn 2p of the $CoMn_2O_4$, (f) Mn 3s of the $MnCo_2O_4$ and $CoMn_2O_4$.

XPS analyses (Fig. 2) are carried out to investigate these porous $MnCo_2O_4$ and $CoMn_2O_4$ microspheres and the valence states of the metal ions. The survey spectrum in Fig. 2a evidences the presence of Mn, Co and O as well as C from the reference. By using a Gaussian fitting method, the Co 2p spectrum (Fig. 2b and c) are best fitted two spin-orbit doublets characteristic of Co^{2+} and Co^{3+} and two shake-up satellites (denoted as sat.).[24-26] The observation of satellite peak near 790 eV in Fig. 2b suggests the presence of Co^{3+}, while the satellite peak at 785 eV reflects the existence of Co^{2+}. Therefore, the Co ions should be a mixed valence of +2 and +3 in the sample of $MnCo_2O_4$. In the Co 2p spectrum (Fig. 2c), two peaks of Co $2p_{3/2}$ and Co $2p_{1/2}$ locate at 780.5 and 795.9 eV and two conspicuous shake-up satellite peaks locate at 786.5 and 802.8 eV, respectively. Revealing the co-existence of Co^{2+} and Co^{3+} in $CoMn_2O_4$. The Mn 2p spectrum (Fig. 2d and e) are obtained under assumption of two pairs of spin-orbit doublets (Mn $2p_{3/2}$ located at ~ 642.0 eV and Mn $2p_{1/2}$ located at ~653.5 eV). After refined fitting, the spectrum can be divided into four peaks. Among them, 641.6 and 653.1 eV can be ascribed to the existence of Mn^{2+}, and other two peaks located at 642.6 and 654.0eV can be assigned to be Mn^{3+}.[27] Therefore, it was concluded that both Mn^{2+} and Mn^{3+} existed in $MnCo_2O_4$ and $CoMn_2O_4$ microspheres. The Mn 3s spectrum in Fig. 2f presents multiplet splitting peaks that result from the exchange interaction between the electrons in 3s and 3d orbital.[28] Magnitude of peak splitting is diagnostic of oxidation state.[29] The magnitude of peak splitting is 5.4 eV, indicates that the average Mn valence is close to +2 in $MnCo_2O_4$, while the peak splitting is 5.9 eV indicating the priority of +3 (Mn valence) in $CoMn_2O_4$.[30,31] In addition, the chemical compositions of porous $MnCo_2O_4$ and $CoMn_2O_4$ microspheres are also analyzed by EDX, which gives the Mn/Co molar ratios of ~0.5 and ~2 (Fig. S1), respectively.

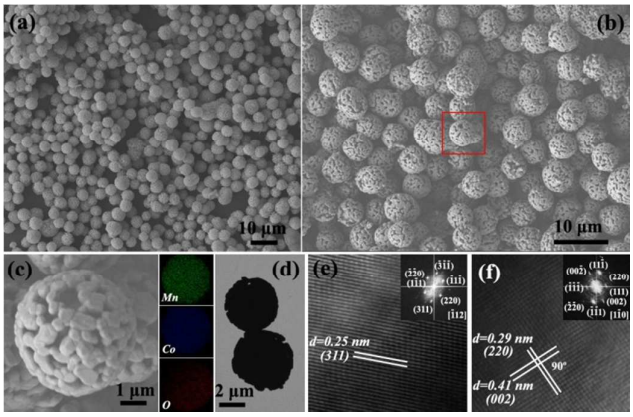

Fig. 3 (a-c) Typical SEM images of the porous $MnCo_2O_4$ microspheres and the corresponding element mappings; (d-f) TEM and HRTEM images of porous $MnCo_2O_4$ microspheres and the corresponding Fourier transform images taken by HRTEM.

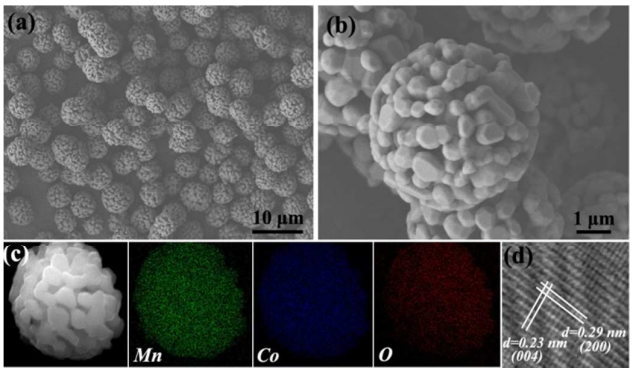

Fig. 4 (a-c) SEM images of the porous $CoMn_2O_4$ microspheres and corresponding element mappings; (d) HRTEM image of the $CoMn_2O_4$ microspheres.

The morphologies and microstructures of the porous $MnCo_2O_4$ and $CoMn_2O_4$ microspheres are further investigated by SEM and TEM, as shown in Fig. 3 and Fig. 4. The low magnified SEM image (Fig. 3a) reveals that a large amount of uniform $MnCo_2O_4$ microspheres is obtained with an average diameter of about 3-6 μm. As shown in Fig. 3b and 3c, each microsphere is composed of numerous polyhedral particles with diameters of ~200-500 nm. The structure of the polyhedral particles is showed in Fig. S2. The broken part of a porous $MnCo_2O_4$ microsphere is shown in Fig. 3b. It is found that the interior of microsphere also composed of small polyhedron particles. These polyhedron particles stacks together compactly through TEM image (Fig. 3d). The elemental mapping image show well matched spatial distributions of Mn, Co and O. High-resolved lattice fringes and corresponding Fourier transform image for the chosen region are shown in Fig. 3e, which displays distinct lattice fringes with an interplanar distance of 0.25 nm, corresponding to the (311) planes spacing of $MnCo_2O_4$ crystal. The lattice fringes could be ascribed to the planes of (220), (311) and (1 $\bar{1}$ 1) according to Fourier transform image. Furthermore, Figure 3f exhibits two groups of vertical crystal planes with lattice spacing of 0.29 and 0.41 nm, which correspond to the planes of (220) and (002), respectively. Several sets of visible lattice fringes are observed by Fourier

transform image, which could be assigned to the planes of (002), (111), (220) and (11 $\bar{1}$).[32]

Fig. 4a and 4b show the SEM images of the $CoMn_2O_4$. The porous $CoMn_2O_4$ are also composed of numerous polyhedral nanoparticles. The elemental mapping image also displays well dispersed Mn and Co elements (Fig. 4c). A representative HRTEM image is shown in Figure 4d, in which the lattice spacing of 0.23 and 0.29 nm correspond to the (004) and (200) crystal planes of tetragonal $CoMn_2O_4$.

A series of contrast experiments were carried out to reveal the growth mechanism of the porous $MnCo_2O_4$ and $CoMn_2O_4$ microspheres. At the initial stage of the experiment, the Mn^{2+} and Co^{2+} dissolved in EG and formed a homogeneous solution. When a certain amount of HMT is added into EG, the HMT might be acted as the soft template. Due to the strong coordination ability of HMT to metal ions through the –N functional groups, the MnCo-complex structure will form.[10] The Mn^{2+} and Co^{2+} ions at high temperature are nucleated under solvothermal conditions and self-assembled into large nanoparticles. It is considered that the HMT (absorbed on the surfaces of nanoparticles) acted as a structure-directing role during the formation of yolk-shell structured MnCo-precursors (Fig. S3). It is also observed that the yolk is composed of larger nanoparticles while the outside shell (Fig. 2b) is made up of smaller ones. This phenomenon shows that the growth of yolk and shell undergo different growth processes. It is speculated that larger MnCo-precursor nanoparticles aggregated together and formed yolk in the initial stage, while the smaller nanoparticles gradually appeared with the decreasing concentration of metal ions and deposited on the surface of yolk, and then formed shell at last. The emergence of a sole yolk (without shell) that is composed of large nanoparticles further evidenced our speculation (Fig. S3c). At last, the reaction of Mn^{2+} and Co^{2+} with HMT in EG solvent at 180 ℃ for 12 h can produce yolk-shell MnCo precursors. The results of IR (Fig. S4), XRD (Fig. S5) and TGA curve (Fig. S6) demonstrate the MnCo precursors are $Mn_{0.33}Co_{0.67}CO_3$ and $Co_{0.33}Mn_{0.67}CO_3$.

During the heat treatment at high temperature, there exists a temperature gradient for the materials, which could produce a large contraction force (*Fc*) and an opposite adhesion force *(Fa*) along the radical direction.[4,33,34] The large contraction force together with the adhesion force provide the driven force for separating microspheres into multilayer structure. Under the action of contraction force, the small nanoparticles aggregated together and formed polyhedral particles at high temperature. The formation of polyhedral particles may be associated with HMT (adsorbed on the surface of small precursor nanoparticles). In the absence of HMT, no polyhedral particles could be obtained. Li et al. reported that the *Fa* exceeds the *Fc* between the inner carbonates and the outer complex oxides at the initial stage of calcinations, generated by the high ramping rate, which results in the formation of porous structures.[4] There are a few works reported the possibilities to create porous materials by controlling the thermal decomposition process.[33,34] After the precursors were calcined for two hours in air atmospheres, porous $MnCo_2O_4$ and $CoMn_2O_4$ microspheres were obtained.

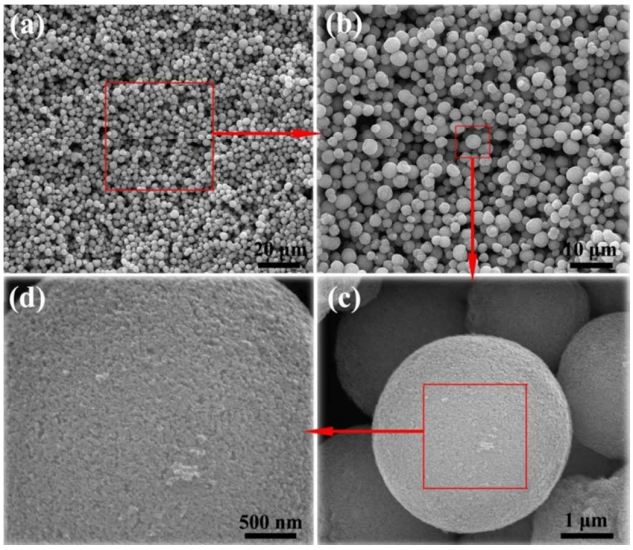

Fig. 5 (a-d) Different magnification of SEM image of $MnCo_2O_4$ microspheres obtained at 600 ℃ for 6 h.

It is worth noting that the calcinations time also play very important role on the shape evolutions of the final products. After $Mn_{0.33}Co_{0.67}CO_3$ was calcined after four hours, the polyhedral nanoparticles gathered more compact. It is also found that some pores disappeared and the yolk structure formed gradually (Fig. S7), which exhibited a transitional state to forming yolk-shell structure renewedly. With the prolonged annealing time, a separate outer shell and an inner solid yolk formed due to the combined effect of contraction and adhesion forces controlled by a heating rate of 10 ℃/min.[4,33] A large amount of uniform $MnCo_2O_4$ yolk-shell microspheres with diameters in the range of 2-4.5 μm is obtained after calcinations for six hours (Fig. 5 and S8). Yolk-shell $Mn_{0.33}Co_{0.67}CO_3$ and $MnCo_2O_4$ microsphere have two obvious differences by SEM observation. First, the enlarged image of the yolk-shell $MnCo_2O_4$ microsphere indicates that the spheres are consisted of numerous nanoparticles with an average size of ~35 nm (Fig. 5d). Second, the size of nanoparticles that constituted of yolk and shell is uniform (Fig. S8), but the sizes of nanoparticles consisted of $Mn_{0.33}Co_{0.67}CO_3$ are varied. The above results further confirmed that the products undergo a particle rearrangement process at high temperature. With the prolonged calcinations, more and more broken microspheres appeared (Fig. S9 and S10). The reason that more broken microspheres emerged might be largely attributed to the long time effect of two kinds of force (*Fc* and *Fa*). From the broken microspheres that showed in Fig. S8 and Fig. S9, the yolk-shell structure with the outer shell and inner yolk can be clearly discerned. The outer shell is about 0.6 μm in thickness and the diameter of the inner yolk is about 1.8 μm. If the calcinations time was exceeded 16 h, the temperature gradient reduced and disappeared gradually at last.[4] At this point, the yolk-shell structure also tends to disappear with the rearranging process. From Fig. S11, one can see that porous structures disappear and yolk and shell merge together gradually if the annealing time

was 16 h. At last, the yolk-shell microspheres rearranged into irregular spheres after annealing for 24 h (Fig. S12). The formation process of the products undergo an evolutionary process of yolk-shell $Mn_{0.33}CO_{0.67}CO_3$, porous $MnCo_2O_4$ microspheres, yolk-shell $MnCo_2O_4$ microspheres and solid microsphere.

Besides the calcinations time, the controllable parameters including reaction time, reaction temperature and HMT are elaborate discussed. Reaction time plays an important role in the formation of porous microspheres and influences the final yield of the products. In the typical procedures, the reaction time stopped at different time (1, 5, 10, 12, 24 h). It is found that no solid powers could be obtained when the reaction time was less than 5 h. When the reaction time was 10 h, MnCo precursor was formed but the yield at this time is lower than that of 12 h while there are no obvious difference on the yield and morphology of the final products when the reaction time was 12 or 24 h. Therefore, we select 12 h as the optimal reaction time for fabricating the precursor materials. Reaction temperature mainly has influences on the yield of the products. No MnCo precursor microspheres could be obtained when the temperature was below 150 ℃. When the reaction time was12 h and temperature was 180 ℃, the yield is the highest compared with those of the product obtained at lower temperature and shorter time. It is found that HMT play crucial role on the formation of spherical MnCo precursor. In the absence of it, only irregular fragments could be obtained (Fig. S13). Once the HMT was added (even if the amount is only 0.1 g), irregular microspheres could be formed (Fig. S14a and 14b). When 0.5 g HMT was used, the final products were mainly composed of irregular microspheres (Fig. S14c). When the mass of HMT exceeds 1.0 g, more and more precursor microspheres appeared. And the highest proportion of the microspheres was obtained when the mass of HMT was 1.5 g (the optimal condition). It is also found that a slight decrease or increase in the amount of HMT (~1.5 g) did not obviously affect the formation of the final precursor. When the mass of HMT exceeds 3.0 g, only solid spheres were obtained (see Figure S14d, e and f).

This schematic growth mechanism and morphology change process of the porous $MnCo_2O_4$ microspheres are proposed in Scheme 1 and Table S1.

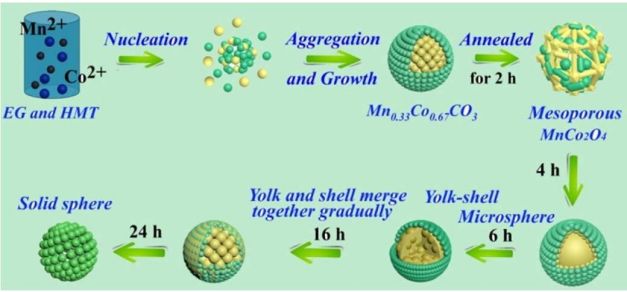

Scheme 1 Schematic illustration of the morphology evolution of the $MnCo_2O_4$ structure for different annealed time.

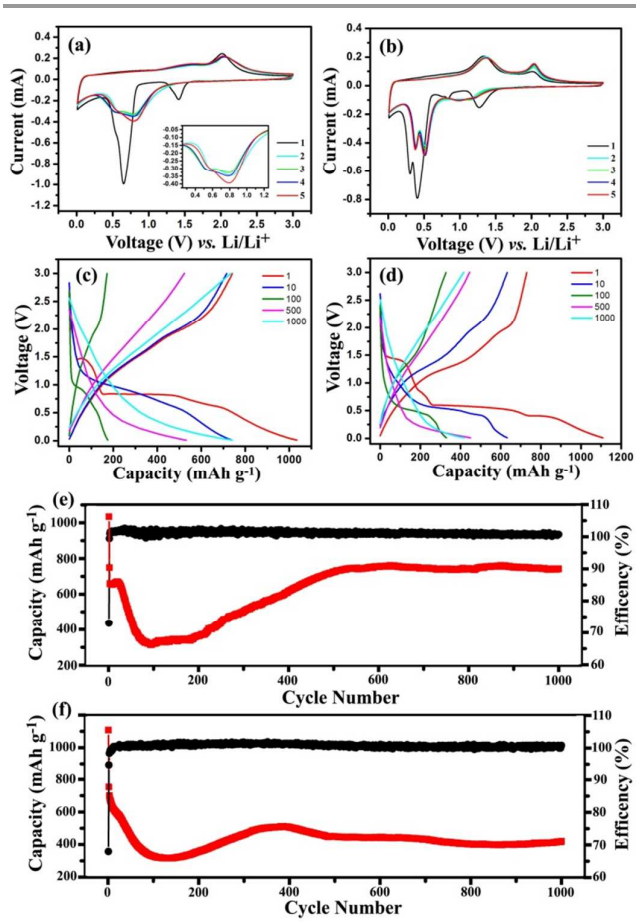

Fig. 6 The first five consecutive CV curves of the (a) $MnCo_2O_4$ and (b) $CoMn_2O_4$ electrodes in the voltage range of 0.01-3.0 V at scan rate of 0.1 mV s^{-1}. The 1st, 10th, 100th, 500th, 1000th cycle discharge/charge curves of the (c) porous $MnCo_2O_4$ and (d) $CoMn_2O_4$ microspheres at current density of 1000 mA g^{-1}. Cycling performance and Columbic efficiency of the porous (e) $MnCo_2O_4$ and (f) $CoMn_2O_4$ microspheres at current density of 1000 mA g^{-1}.

The electrochemical properties of the porous $MnCo_2O_4$ and $CoMn_2O_4$ microspheres are firstly evaluated by CV and discharge/charge process, as shown in Fig. 6. Fig. 6a and 6b show the first five CV curves of the $MnCo_2O_4$ and $CoMn_2O_4$ electrode in the voltage range of 0.01-3.0 V at a scan rate of 0.1 mVs^{-1}. In the first cycle, as shown in Fig. 6a, a broad peak centered at ~1.41 V could be attributed to the reduction of Co^{3+} to Co^{2+}. A sharp peak located at ~0.60 V could be assigned to the further reduction of Co^{2+} and Mn^{2+} to metallic Co and Mn, respectively.[22] These irreversible reduction processes can be described by the following equation (1):

$$MnCo_2O_4 + 8Li^+ + 8e^- \rightarrow Mn + 2Co + 4Li_2O \quad (1)$$

In the anodic scan, two broad oxidation peaks are observed at 1.60 V and 2.02 V, which corresponded to the oxidation of Mn to Mn^{2+} and Co to Co^{2+}, respectively.[6] In the second and fifth cycles, it can be observed the reduction peak at 0.6 V is moved to ~0.80 V and become broader, and a small peak centered at ~0.52 V appeared. This peak may be seen indistinctly in the first cycles because this weak peak overlapped with the intense sharp peak at ~ 0.60 V. It is also find that the peak centered at

0.60 V moved to 0.80 V in the second cycles, and then the peak at 0.52 V appeared gradually. The second five cycles are characterized by two pairs of redox peaks. The one at 0.52/1.60 V corresponds to the reduction/oxidation of MnO/Mn, while the other one at 0.79/2.04 V is assigned to the reduction/oxidation of CoO/Co.[32] This redox process can be described as the following equation (2):

$$Mn + 2Co + 3Li_2O \leftrightarrow MnO + 2CoO + 6Li^+ + 6e^- \quad (2)$$

Different from the electrochemical behaviour of $MnCo_2O_4$, the $CoMn_2O_4$ electrode exhibits two obvious peaks at 0.30 and 0.40 V in the first reduction sweep, as shown in Fig. 6b, which could be assigned to the reduction of Co^{2+} to Co and Mn^{2+} to Mn, respectively. In the following cycles, these two peaks shift at 0.37 and 0.51 V. The peak centered at 1.25 V could be attributed to the reduction of Mn^{3+} to Mn^{2+}, while the minor peak at ~0.84 V can be ascribed to the irreversible decomposition of solvent in the electrolyte to form the solid electrolyte interface (SEI).[4] On the basis of these reduction CVs, the electrochemical process can be described as followed equation (3):

$$CoMn_2O_4 + 8Li^+ + 8e^- \rightarrow Co + 2Mn + 4Li_2O \quad (3)$$

In addition, there are two oxidation peaks (1.35 and 2.02 V) in the anodic sweep, which is due to the oxidation of Co to Co^{2+} and Mn to Mn^{2+}, respectively.[4] From the second cycles, the repeated reduction/oxidation process at 0.37/1.35 V corresponds to the MnO/Mn, and the process at 0.51/2.02 V corresponds to the CoO/Co. These reversible redox processes can be described by the following equation (4):

$$Co + 2Mn + 3Li_2O \leftrightarrow CoO + 2MnO + 6Li^+ + 6e^- \quad (4)$$

The discharge/charge curves of the porous $MnCo_2O_4$ and $CoMn_2O_4$ microspheres for the 1st, 10th, 100th, 500th and 1000th cycles at a current density of 1000 mA g^{-1} are shown in Fig. 6c and 6d. The initial discharge and charge capacities of $MnCo_2O_4$ and $CoMn_2O_4$ are 1034 and 749 mAh g^{-1}, 1107 and 750 mAh g^{-1}, corresponding to 72% and 68% of the first coulombic efficiency. The initial discharge capacities are higher than their theoretical values (906, 921 mAh g^{-1}). The formation of SEI on the electrode interface may contribute to the extra capacity at the first cycle. Fig. 6e shows the cycling performance of the porous $MnCo_2O_4$ microspheres at 1000 mA g^{-1}. Despite the porous structure of the $MnCo_2O_4$, the capacity fading is obviously from 690 mAh g^{-1} (at the 10th cycle) to 350 mAh g^{-1} (at the 100th cycle). Porous metal oxide spheres as electrodes still suffer severe mechanical degradation due to the volume change inherently accompanying with conversion reaction. The repetitive volume expansion/contraction can fracture the SEI layers and expose new active surfaces for SEI growth during discharge/charge process. These reasons can lead to tremendous capacity fading, particularly at high current density rate.[34-39] Amazingly, after capacity fading to the lowest value at the 100th cycle, increased Li storage sequentially during the subsequent cycles without signs of further decay. The capacity can reach 740 mAh g^{-1} at the 550th cycle and remain stable until 1000 cycles. Sun et al. proved the causes of similar phenomenon is that high-rate lithiation-induced reactivation can occur for the porous hollow sphere metal oxide electrodes in which lithiation-induced mechanical degradation can effectively restructure the porous sphere and optimize stable SEI.[35] With the structure refinement and formation of a stable SEI, the reactivated electrode exhibits an excellent reversible capacity and an unprecedented cycling stability without capacity decay after an extremely long cycle at high rates.[40] Although stable SEI was not found after 200 charge-discharge cycles (Fig. S16), however, large-area stable SEI appeared after 1000 cycles (Fig. S17) and particle (structure) refinement process were observed under SEM (Fig. S16). The capacity fading and reactivation process of the porous $MnCo_2O_4$ microspheres are affected significantly by different current density rates. At a lower rate of 200 mA g^{-1}, electrodes experience less capacity fading and short capacity reactivation, and the reactivation process can be completed at ~150 cycles (Fig. S18). The porous $CoMn_2O_4$ microspheres also display a similar cycle process. The capacity decreased from 630 mAh g^{-1} (at the 10th cycle) to 310 mAh g^{-1} (at the 120th cycle) at 1000 mA g^{-1}. After the capacity fading to the lowest value at 120th cycles, the capacity can reach 420 mAh g^{-1} in the next 280 cycles, and the capacity remains stable until 1000 cycles. By comparison with the $MnCo_2O_4$ and $CoMn_2O_4$ samples, $MnCo_2O_4$ exhibits a long reactivation process and a high reversible capacity in the discharge/charge cycles at high current density. One possible reason may be due to the larger surface area of $MnCo_2O_4$ experienced more severe fracture of SEI layers caused by volume expansion/contraction during cycles. According to the N_2 adsorption/desorption results, the porous $MnCo_2O_4$ and $CoMn_2O_4$ microspheres give rise to Brunauer-Emmett-Teller specific surface area of 28.45 and 19.61 $m^2 g^{-1}$ (Fig. S19). Therefore, formation optimized stable SEI layers need more cycles. Furthermore, large surface area of $MnCo_2O_4$ could supply more Li^+ insertion/extraction sites, which is beneficial to improve the capacity of the electrode.

The comparison performances of the different structures such as porous microspheres, yolk-shell microspheres and solid microspheres of $MnCo_2O_4$ and $CoMn_2O_4$ were carried out. It is found that yolk-shell microspheres exhibited similar cycling performance trend but their specific capacity slightly lower than those of $MnCo_2O_4$ and $CoMn_2O_4$ porous microspheres. The yolk-shell $MnCo_2O_4$ microspheres are also consisted of numerous nanoparticles with an average size of ~35 nm, which has a bigger volume effect than that of porous microspheres owing to their closely packed nanoparticle structures. Therefore, the capacity of yolk-shell microspheres is slightly lower than that of porous microspheres especially in long cycles at high rate. The discharge capacities of yolk-shell $MnCo_2O_4$ and $CoMn_2O_4$ microspheres are 650 mAh g^{-1} and 320 mAh g^{-1} at 1000 mA g^{-1} after 600 cycles, higher than that of $MnCo_2O_4$ solid microspheres (Fig. S15).

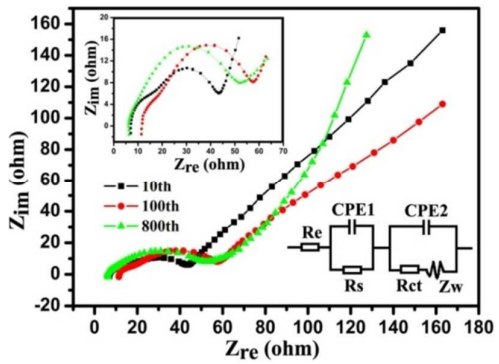

Fig. 7 Nyquist plots of the 10, 100 and 800 cycles and corresponding to the Equivalent circuit (inset).

EIS considered as one of the most sensitive tools for the study of electrochemical behaviour due to the surface modification.[41] The Nyquist plots of $MnCo_2O_4$ electrode at different cycle stages (10th, 100th and 800th) are exhibited in the EIS. The electrochemical property of lithiation-induced reactivation and stable SEI formation process can be acquired from Nyquist plots. The Nyquist plots are composed of two semicircles overlap each other in the high and middle frequency regions and incline lines in the low frequency, which are relative to the SEI resistance (R_s), charge-transfer resistance (R_{ct}) and the Warburg impedance of the Li ion diffusion in the solid materials, respectively. The kinetic properties are further analyzed by Zsimpwin software, these impedance data (Table 1) are fitted to the equivalent circuit shown in Fig. 7 inset. The diffusion coefficient values of the Li ions for diffusion into the bulk electrode materials could be calculated using the following equation:[42,43]

$$D = 0.5(RT/AF^2C\sigma)^2$$

$$Z_{re} = R_D + R_L + \sigma\omega^{-1/2}$$

Herein, R is the gas constant, T is the absolute temperature, A is the surface area of the electrode, F is the Faraday constant, C is the concentration of lithium ions, σ is the Warburg impedance coefficient which is associated with Z_{re}, ω is the angular frequency in the low frequency, R_D and R_L are the diffusive resistance and liquid resistance, respectively.

Table 1 Electrochemical impedance parameters of the $MnCo_2O_4$ electrode at different cycles.

Cycles	Re (Ω)	Rs (Ω)	Rct (Ω)	σ (Ω cm^{2}S$^{-0.5}$)	D_{Li+}(cm^2 S^{-1})
10th	6.4	4.1	38.9	47.1	1.0E-14
100th	7.3	34.7	60.9	112.8	1.8E-15
800th	12.1	7.0	51.6	29.4	2.7E-14

As shown in Fig. 7 and Table 1, the larger diameter of the semicircle in 100th cycle than those of 10th or 800th cycle suggests larger contact and charge-transfer resistance, which demonstrated that a high resistance and fracture SEI layers was formed on the surface of $MnCo_2O_4$ electrode.[35] Furthermore, both surface film resistance R_s and charge-transfer resistance R_{ct} at 100th cycle are significantly higher than these at 10th and 800th cycle. It is further confirmed that the $MnCo_2O_4$ suffer mechanical degradation due to volume change accompanying with fracture SEI layers, which could lead to R_{ct} increased and weakened Li^+ ion diffusionrate.[31] With the structure refinement and stable thinner SEI formed, the R_{ct} and Li ion diffusion become more superior, and the $MnCo_2O_4$ electrode exhibit enhanced and excellent long-lived cycling performance. This comparison indicates that the lithiation structure refinement and optimization SEI process really exist in the discharge-charge cycles.

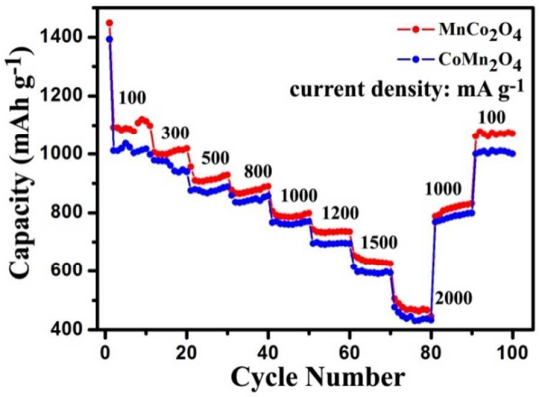

Fig. 8 Rate capabilities of $MnCo_2O_4$ and $CoMn_2O_4$ at different current densities.

To investigate the rate capability of the $MnCo_2O_4$ and $CoMn_2O_4$, the discharge test was evaluated at different current densities ranging from 100 to 2000 mAh g^{-1} (Fig. 8). The $MnCo_2O_4$ electrode shows an average discharge capacity of 1100, 920, 820, 650, 490 mAh g^{-1} at current densities of 100, 500, 1000, 1500, and 2000 mA g^{-1}, respectively. Even when the current density was set as high as 2000 mA g^{-1}, a capacity of about 490 mAh g^{-1} was still available. The discharge capacity decreased slightly with increasing current density. More importantly, the discharge capacity was able to return to 900 and 1100 mAh g^{-1} when the current density went back to 1000 and 100 mA g^{-1}. The $CoMn_2O_4$ electrode showed a similar trend during the rate capability test but the capacity slightly lower than that of $MnCo_2O_4$ electrode at different current densities. It is found that the pulverization degree of $CoMn_2O_4$ is more serious than that of $MnCo_2O_4$ after 200 cycles (Fig. S16). Due to the Jahn-Teller effect and partly dissolution of Mn ions, parts of structure evolution and volume changes of $CoMn_2O_4$ and $MnCo_2O_4$ are inevitable during long cycles. As less Mn content in $MnCo_2O_4$ than that in $CoMn_2O_4$, $MnCo_2O_4$ exhibits relative high structure and cycle stability, especially at high current densities. These results show that the $MnCo_2O_4$ and $CoMn_2O_4$ anode materials have significantly high capacity retention and good rate performance for LIBs. In addition, a comparison of the cycling performance between porous $MnCo_2O_4$ ($CoMn_2O_4$) and other $MnCo_2O_4$ ($CoMn_2O_4$) nanostructures previously reported, as summarized in Table S2. It is obvious that the porous $MnCo_2O_4$ and $CoMn_2O_4$ exhibit high reversible capacity in the long cycles even at high rate density.

4. Conclusions

In summary, a facile solvothermal route has been designed to fabricate uniform yolk-shell $Mn_{0.33}Co_{0.67}CO_3$ and $Co_{0.33}Mn_{0.67}CO_3$ microspheres by tuning the ratio of Mn/Co. After calcined at 600 ℃ for 2 h, the porous $MnCo_2O_4$ and $CoMn_2O_4$ could be obtained. It is worth noting that porous $MnCo_2O_4$ and $CoMn_2O_4$ are composed of numerous polyhedron nanoparticles with diameter of 200-500 nm. When evaluated as anode materials for LIBs, the $MnCo_2O_4$ and $CoMn_2O_4$ exhibit a superior electrochemical performance. The lithiation-induced restruction and SEI optimization demonstrated by EIS at different stage during discharge/charge process. After undergo this restruction process, the electrodes exhibit a long-lived stability. For instance, the porous $MnCo_2O_4$ and $CoMn_2O_4$ display high reversible capacities of 740 and 420 mAh g^{-1} after 1000 cycles at current density of 1000 mA g^{-1}. The excellent performances of porous $MnCo_2O_4$ and $CoMn_2O_4$ microspheres enable it to be a new candidate for next-generation of energy storage and conversion devices.

Acknowledgements

This work was supported by the 973 Project of China (No. 2011CB935901), National Natural Science Foundation of China (Nos. 21301102，21471091 and 1179043), the Scientific Research Foundation of Shandong Province Outstanding Young Scientist Award (No. BS2013CL023) and the Fundamental Research Funds of Shandong University (No. 2015JC007).

Notes and references

1 R.R. Zhang, A.H. Li and L. Q. Xu, *Nanoscale* 2014, **6**, 14221.
2 X. J. Hou, X. F. Wang, B. Liu, Q. F. Wang, T. Luo, D. Chen and G. Z. Shen, *Nanoscale*, 2014, **6**, 8858.
3 G. Z. Yang, H. Cui, G. W. Yang and C. X. Wang, *ACS Nano*, 2014, **8**, 4474.
4 J. F. Li, S. L. Xiong, Y. R. Liu, Z. C. Ju and Y. T. Qian, *ACS Appl. Mater. Interfaces*, 2013, **5**, 981.
5 R. R. Zhang, Y.Y. He and L. Q. Xu *J. Mater. Chem. A*, 2014, **2**, 17979.
6 S. X. Jin and C. X. Wang, *Nano Energy*, 2014, **7**, 63.
7 H. Long, T. L. Shi, S. L. Jiang, S. Xi, R. Chen, S. Y. Liu, G. L. Liao and Z. R. Tang, *J. Mater. Chem. A*, 2014, **2**, 3741.
8 L. Zhou, D. Y. Zhao and X. W. Lou, *Adv. Mater.*, 2012, **24**, 745.
9 G. R. Yang, X. Xin, W. Yan, H. H. Yang and S. J. Ding, *Electrochimica Acta*, 2014, **137**, 462.
10 K. Uusi-Esko, E. L. Rautanma, M. Laitinen, T. Sajavaara and M. Karppinen, *Chem. Mater.*, 2010, **22**, 6297.
11 T. Y. Ma, Y. Zheng, S. Dai, M. Jaroniec and S. Z. Qiao, *J. Mater. Mater. A*, 2014, **2**, 8676.
12 W. Y. Li, K. Xu, G. S. Song, X. Y. Zhou, R. Zou, J. M. Yang, Z. G. Chen and J. Q. Hu, *CrystEngComm*, 2014, **16**, 2335.
13 S. G. Mohamed, T. F. Hung, C. J. Chen, C. K. Chen, S. F. Hu and R. S. Liu, *RSC Adv.*, 2014, **4**, 17230.
14 J. F. Li, S. L. Xiong, X. W. Li and Y. T. Qian, *Nanoscale*, 2013, **5**, 2045.
15 J. M. Tarascon and M. Armand, *Nature*, 2001, **414**, 359.
16 L. Yu, H. B. Wu, G. Q. Zhang and X. W. Lou, *Energy Environ. Sci.*, 2013, **6**, 2664.
17 P. G. Bruce, B. Scrosati and J. M. Tarascon, *Angew. Chem. Int. Ed.*, 2008, **47**, 2930.
18 G. M. Zhou, F. Li and H. M. Cheng, *Energy Environ. Sci.*, 2014, **7**, 1307.
19 J. Gao, G. Liang, B. Zhang, Y. Kuang, X. Zhang and B. Xu, *J. Am. Chem. Soc.*, 2007, **129**, 1428.
20 G. Z. Yang, H. W. Song, H. Cui and C. X. Wang, *Nano Energy*, 2014, **5**, 9.
21 A.H. Li, L.Q. Xu, S.L. Li, Y.Y. He, R.R. Zhang and Y.J. Zhai, *Nano Research* 2015, **8**(2): 554.
22 Y. J. Zhai, X. J. Ma, H. Z. Mao, W. W. Shao, L.Q. Xu, Y. Y. He and Y. T. Qian, *Adv. Electron. Mater.*，2015，1400057.
23 S. L. Li, A. H. Li, R. R. Zhang, Y. Y. He, Y. J. Zhai and L. Q. Xu, *Nano Research*, 2014, **7**, 1116.
24 C. V. Schenck, J. G. Dillard and J. W. Murray, *J. Colloid Interface Sci.*, 1983, **95**, 398.
25 M. Oku and Y. Shao, *Appl. Surf. Sci.*, 1992, **55**, 37.
26 S. A. Needham, G. X. Wang, K. Konstantinov, Y. Tournayre, Z. Lao and H. K. Liu, *Electrochem. Solid-State Lett.*, 2006, **9**, A315.
27 B. J. Tan, K. J. Klabunde and P. M. A. Sherwood, *J. Am. Chem. Soc.*, 1991, **113**, 855.
28 E. Z. Kurmaev, M. A. Korotin, V. R. Galakhov, L. D. Finkelstein, E. I. Zabolotzky and N. N. Efremova, *Phys. Rev. B*, 1999, **59**, 12799.
29 J. P. Liu, J. Jiang, M. Bosman and H. J. Fan, *J. Mater. Chem.*, 2012, **22**, 2419.
30 M. Chiganc and M. Ishikawa, *J. Electrochem. Soc.*, 2000, **147**, 2246.
31 J. M. Cerrato, M. F. Hochella, J. W. R. Knocke, A. M. Dietrich and T. F. Cromer, *Environ. Sci. Technol.*, 2010, **44**, 5881.
32 C. C. Fu, G. S. Li, D. Luo, X. S. Huang, J. Zheng and L. P. Li, *ACS Appl. Mater. Interfaces*, 2014, **6**, 2439.
33 G. Q. Zhang, L. Yu, H. B. Wu, H. E. Hoster and X. W. Lou, *Adv. Mater.*, 2012, **24**, 4609.
34 C. C. Yu, L. X. Zhang, J. Shi, J. Zhao, J. Gao and D. S. Yan, *Adv. Funct. Mater.*, 2008, **18**, 1544.
35 H. T. Sun, G. Q. Xin, T. Hu, M. P. Yu, D. Shao, X. Sun and J. Lian, *Nature Commun.*, 2014, **5**, 1.
36 Y. G. Wang, Z. S. Hong, M. D. Wei and Y. Y. Xia, *Adv. Funct. Mater.*, 2012, **22**, 5185.
37 Z. Hu, L. X. Wang, K. Zhang, J. B. Wang, F. Y. Cheng, Z. L. Tao and J. Chen, *Angew. Chem. Int. Ed.*, 2014, **53**, 1.
38 Y. Z. Jiang, D. Zhang, Y. Lo, T. Z. Yuan, N. Bahlawane, C. Liang, W. P. Sun, Y. H. Lu and M. Yan, *Nano Energy*, 2014, **4**, 23.
39 N. Zhang, Q. Zhao, X. P. Han, J. G. Yang and J. Chen, *Nanoscale*, 2014, **6**, 2827.
40 M. H. Chen, J. L. Liu, D. L. Chao, J. Wang, J. H. Yin, J. Y. Lin, H. J. Fan and Z. X. Shen, *Nano Energy*, 2014, **9**, 364.
41 A. Y. Shenouda and H. K. Liu, *J. Electrochem. Soc.*, 2010, **157**, A1183.
42 L. Wang, J. S. Zhao, X. M. He and C. R. Wan, *Electrochim. Acta*, 2011, **56**, 5252.
43 X. Chen, N. Q. Zhang and K. N. Sun, *J. Mater. Chem.*, 2012, **22**, 13637.

Fabrication of hierarchical porous $MnCo_2O_4$ and $CoMn_2O_4$ microspheres that are composed of polyhedral nanoparticles as promising anodes for long-life LIBs

Guangda Li, Liqiang Xu,* Yanjun Zhai and Yaping Hou

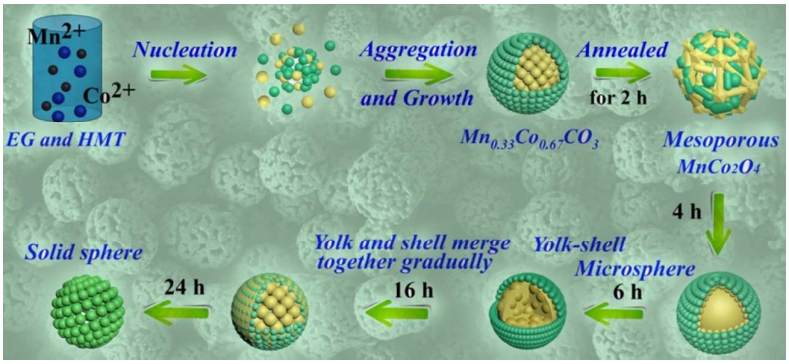

Uniform mesoporous $MnCo_2O_4$ and $CoMn_2O_4$ microspheres that are consisted of numerous polyhedral nanoparticles were prepared and further evaluated as anode materials for lithium-ion batteries, which exhibited excellent long-life cycling stability at high rate density.